



CHALMERS
UNIVERSITY OF TECHNOLOGY

Preparation and lithium storage performance of SiO₂/Ag composite materials coated with polyphosphazene

Downloaded from: <https://research.chalmers.se>, 2025-06-17 15:28 UTC

Citation for the original published paper (version of record):

Zhao, Z., Xu, Z., Zheng, Z. et al (2024). Preparation and lithium storage performance of SiO₂/Ag composite materials coated with polyphosphazene. *Express Polymer Letters*, 18(10): 976-990.
<http://dx.doi.org/10.3144/expresspolymlett.2024.75>

N.B. When citing this work, cite the original published paper.

Research article

Preparation and lithium storage performance of SiO₂/Ag composite materials coated with polyphosphazene

Zhengping Zhao¹, Zhao Xu², Zhong Zheng¹, Wei Wang¹, Wenyu Wang¹, Xingcheng Yang¹, Siqi Zhu¹, Jia Wei Chew^{3*}

¹Zhijiang College, Zhejiang University of Technology, 310024 Hangzhou, P.R. China

²College of Materials Science and Engineering, Zhejiang University of Technology, 310014 Hangzhou, P.R. China

³Chemical Engineering, Chalmers University of Technology, 412 96, Gothenburg, Sweden

Received 14 May 2024; accepted in revised form 2 July 2024

Abstract. Lithium-ion batteries (LIBs) are widely used as important energy storage and energy supply devices. The porous design and heteroatomization modification of carbon-based anode materials are crucial for achieving high-capacity and reversible energy storage in LIBs. Sol-gel method and pyrolysis treatment were used to obtain silica/silver composite particles used as templates. Polyphosphazene-coated silica/silver composite carbon materials (SiO₂/Ag@PZS-C) were synthesized through *in-situ* self-assembly and carbonization of polyphosphazene. The electrochemical behavior and lithium storage mechanism of SiO₂/Ag@PZS-C was also studied.

The results reveal that the composite exhibited high specific capacity, stable cycling and superior rate performance. The double modification of silver nanoparticles and polyphosphazene carbon significantly improves the conductivity of silica and reduces the volume change. Moreover, the carbon shell of polyphosphazene facilitated the formation of a stable solid electrolyte interface film (SEI), preventing direct contact between the active material and the electrolyte, thereby substantially enhancing lithium storage performance.

Keywords: lithium-ion battery, silica, polyphosphazenes, PAN, anode material

1. Introduction

The energy crisis is a prominent and critical issue which hinges on the development of new energy sources, as well as advancements in energy storage and distribution. In recent years, there has been rapid progress in the development and research of renewable and clean energy sources like solar, biomass, and wind energy. However, the associated low energy storage and conversion efficiency, susceptibility to weather constraints, and other significant issues impede their widespread adoption. Converting electrical energy into chemical energy for storage is crucial for the effective utilization of new energy sources. Lithium-ion batteries offer numerous advantages over conventional rechargeable batteries,

including high specific energy, extended cycle life, minimal self-discharge, elevated working voltage, environmental friendliness, and the absence of memory effect. Consequently, they find widespread applications in mobile phones, electric vehicles, and large-scale smart grids [1].

Lithium-ion batteries (LIBs) represent a type of secondary battery (*i.e.*, electrically rechargeable), like nickel-metal hydride, nickel-chromium, and lead acid batteries. Lithium-ion batteries offer several advantages over conventional secondary batteries, such as extended cycle life, high energy density, safety, and non-toxicity [2]. Specifically, the nominal voltage of lithium-ion batteries is three times that of nickel-chromium and nickel-metal hydride batteries.

*Corresponding author, e-mail: jia.chew@chalmers.se

© BME-PT

Typically, lithium-ion batteries can undergo over 500 charging and discharging cycles, satisfying the long-term needs of low-power appliances. Moreover, lithium-ion batteries exhibit significantly better safety compared to lithium-metal batteries, greatly reducing the risk of lithium dendrite penetration. Furthermore, lithium-ion batteries do not contain cadmium, lead, or other harmful elements, resulting in reduced environmental pollution.

Polyphosphazenes (PZS) are organic-inorganic hybrid polymers characterized by alternating phosphorus and nitrogen atoms in the main chain, with various substituents in the side chain branches. Polyphosphazenes can be structurally divided into linear, cyclic, and other unique structures [3, 4]. Owing to the main chain's high flexibility and the design flexibility of side groups, linear polyphosphazenes demonstrate outstanding characteristics, including water solubility, resistance to high and low temperatures, optical transparency, photothermal stability, bio-compatibility [5], flame retardancy, and non-flammability [6]. Cross-linked polymers exhibit superior thermal, structural, and solvent stability compared to linear polyphosphazenes. Cyclic cross-linked polyphosphazene is synthesized through the polycondensation of hexachlorocyclophosphazene with another multi-reactive monomer. It is noteworthy that, besides the main chain structure, the properties of side groups significantly influence the characteristics of polyphosphazenes and their derivatives. This is fundamentally due to the high chemical reactivity of chlorine atoms bonded to phosphorus atoms within the polyphosphazene unit. Through nucleophilic substitution, various functional groups such as alkyl, ethoxy, phenoxy, and amino groups can be introduced to synthesize polyphosphazenes with diverse or even opposing properties. This remarkably broadens the application spectrum of polyphosphazenes, ranging from elastomers to glasses, from biological inertness to bioactive materials [7], and from electronic insulators to conductive materials [8, 9], fully showcasing the functional versatility of polyphosphazenes.

Silica exhibits a higher theoretical specific capacity compared to graphite materials. Silicon dioxide, in contrast to elemental silicon, offers enhanced cycling stability and is readily available from diverse sources, with low toxicity and cost. Currently, nano-SiO₂ is primarily prepared using methods such as reverse microemulsion and the sol-gel technique.

Among these methods, the sol-gel process stands out for its simplicity, low cost, and ability to produce nano-SiO₂ with excellent dispersion.

However, a major drawback hindering high-performance applications of SiO₂ is its inherently low electronic conductivity. Various methods, including the use of hollow porous materials [2], carbon coating [10], and modification with conductive materials [11], have been explored to enhance the conductivity of silica. However, the outcomes have been unsatisfactory. As we all know, the introduction of metal particles with good conductivity can effectively reduce the charge transfer resistance of electrode materials, and silver is the representative of metal with good conductivity. Based on the exceptional conductivity of silver material, some researchers have attempted to enhance conductivity by modifying SiO₂ with silver nanoparticles using a silver mirror reaction. Silver nitrate is easy to be reduced to elemental Ag due to its strong oxidation, light sensitivity and thermal decomposition, so Ag nanoparticles are usually prepared by reducing AgNO₃. For example, YOO used butylamine as a reducing agent to reduce silver nitrate to obtain Ag [12]. Huang reduced AgNO₃ into nano-Ag by photocatalytic reduction method and deposited it on the surface of composite materials [13, 14]. Furthermore, direct exposure of SiO₂ active materials to the electrolyte can lead to the formation of unstable solid electrolyte interface (SEI) films.

To address this, this study describes the preparation of nanometer-scale SiO₂/AgNO₃ via the sol-gel method, employing ammonia as a catalyst and silver nitrate as an additive. This mixture is then used as a template for the *in-situ* self-assembly of polyphosphazene-coated SiO₂/AgNO₃. Subsequently, SiO₂/Ag@PZS-C is obtained via high-temperature pyrolysis. This study investigates the physicochemical, electrochemical, and lithium storage mechanisms of porous composite materials employed as negative electrodes for LIBs.

2. Experimental section

2.1. Preparation of SiO₂ and SiO₂/Ag

Nano-SiO₂ was prepared by the sol-gel method. Firstly, Solution A was prepared by mixing 10 ml of ethanol (AR, Chemical Book, Shanghai, China), 20 ml of deionized water, and different volumes (namely, 1.85, 3.7, and 7.4 ml) of ammonia (AR, Sinopharm, Shanghai, China) and stirring at room

temperature, while Solution B was prepared by dissolving 3.5 ml of ethyl orthosilicate (TEOS) (AR, Sinopharm, Shanghai, China) in 35 ml of ethanol and stirring at room temperature. Then, Solution B was added to Solution A, and stirring continued for 2 h. After that, the product was separated using a high-speed centrifuge (HC-3514, Zonkia, Anhui, China) and washed three times with anhydrous ethanol, and the obtained product was dried under vacuum at 60 °C for 24 h and then ground into fine powder.

The preparation of SiO₂/Ag was similar to the above, except that a specific concentration of AgNO₃ (AR, Aladdin, Shanghai, China) solution was added to Solution A, and the molar ratio of AgNO₃ to TEOS was 0.1:1. The remaining steps were the same as above. Finally, the obtained product was vacuum-dried at 60 °C for 24 h, ground into a fine powder, and then heat-treated in a tube furnace under an argon atmosphere at 800 °C for 2 h to obtain SiO₂/Ag.

2.2. Preparation of SiO₂@PZS-C and SiO₂/Ag@PZS-C

Due to the significant impact of solvent polarity on the synthesis reaction of polyphosphazene, tetrahydrofuran (AR, Sinopharm, Shanghai, China) with weaker polarity was selected as the main solvent here. The specific experimental steps are described as follows. Firstly, with the prepared SiO₂ as the external template, hexachlorocyclophosphazene (HCCP) (AR, Aladdin, Shanghai, China) and 4,4'-dihydroxydiphenylsulfone (BPS) (AR, Aladdin, Shanghai, China) were added at a molar ratio of 1:3 to a mixture of 75 ml of tetrahydrofuran and 75 ml of ethanol. The mixture was mechanically stirred in an ultrasonic bath at 25 °C and 300 W for 30 min to ensure uniform dispersion. Subsequently, 10 ml of triethylamine was quickly added, and mechanical stirring continued for 120 min under the same ultrasound conditions. After that, the solids were obtained by centrifugation at a speed of 3000 rpm and washed three times with deionized water and ethanol. After washing, vacuum drying at 60 °C overnight was carried out to prepare polyphosphazene-coated silica composite, denoted as SiO₂@PZS. Finally, the composite material was carbonized at 800 °C for 2 h in a tube furnace filled with high-purity argon gas to obtain SiO₂@PZS-C. The preparation process of SiO₂/Ag@PZS-C was similar to that of SiO₂@PZS-C, except SiO₂ was replaced with SiO₂/Ag.

2.3. Sample characterization

The surface morphology of the sample was observed by scanning electron microscope (SEM, Hitachi S-4700, Hitachi, Ltd., Tokyo, Japan). The coating condition of the sample was observed by transmission electron microscope (TEM, JEM-2100F, JEOL Ltd., Tokyo, Japan). The structure of the material after heat treatment was analyzed by X-ray diffractometer (XRD, X' Pert-PRO MPD, PANalytical B.V., Almelo, Netherlands). The scanning range was 5–90°, and the scanning rate was 2°·min⁻¹. The pore structure and pore-forming mechanism of composites were evaluated by automatic specific surface and porosity analyzer (BET, ASAP-2460, Micromeritics, Atlanta, America) and thermogravimetric analyzer (TG, TG 209 F3 Tarsus, NETZSCH, Sable, German). The lattice defects and graphitization degree of carbon materials are analyzed by laser Raman spectrometer (Renishaw InVia, Renishaw, London, UK), and the value of I_D/I_G can be used to characterize the graphitization degree of materials. The surface chemical composition of the material was analyzed by X-ray photoelectron spectroscopy (XPS, Thermo Scientific K-Alpha, Thermo Fisher Scientific, Massachusetts, America).

2.4. Electrochemical test

The electrode sheet is made of active substances, acetylene black (Battery Grade, Sinero, Suzhou, China) and Polyvinylidene fluoride (PVDF) (Battery Grade, Arkema, Suzhou, China) in the weight ratio of 8:1:1, which are stirred into slurry and coated on copper foil (AR, Shenzhen Kejing, Shenzhen, China), dried and cut by button cell slicer (MSK-T10, Shenzhen Kejing, Shenzhen, China). CR2025 button battery was assembled in a glove box (VGB-6, Shenzhen Kejing, Shenzhen, China) filled with argon. The cycle performance and rate performance of the button battery were tested on a high-performance battery testing system (CT-4008-5V10Ma-164, Neware, Shenzhen, China). Cyclic voltammetric curve test and electrochemical impedance test were carried out on the electrochemical workstation (RST5202F, Shiruisi Instrument Technology Co., Ltd, Zhengzhou, China) using a three-electrode system, in which the voltage range of cyclic voltammetric test was 0.01–3 V, the scanning rate was 0.1 mV·s⁻¹, and the frequency range of electrochemical impedance test was 0.01 Hz~100 000 Hz, and the amplitude was 5 mV.

3. Results and discussion

3.1. Structural characterization of composite materials

During the charging cycle, the significant changes in the volume of the silicon material cause it to fall off the current collector, which loses the electrical activity [15]. Studies have demonstrated that smaller silica particle sizes are more effective in mitigating volume expansion effects during charging and discharging processes. Consequently, silica nanoparticles with different particle sizes were prepared by adjusting the concentration of ammonia. The scanning electron microscopy (SEM) images in Figures 1a–1c depict the nano-silica obtained with increasing ammonia volumes of 1.85, 3.7, and 7.4 ml, respectively, indicating excellent overall dispersion with no agglomeration. The average silica particle size was determined using the Nanomeasor software. In Figure 1a, the silica particle size distribution ranges from 100 to 150 nm, with an average size of 126 nm. In Figure 1b, and Figure 1c, the average particle sizes of silica are slightly larger at 174 and 218 nm, respectively. Therefore, with the increase in ammonia concentration, the particle size of the prepared nano-silica also increases accordingly. This is mainly because ammonia as a catalyst promotes the hydrolysis of TEOS and the growth of particles, and this promotion is more significant with the increase of ammonia concentration.

SEM images in Figure 1d, and Figure 1e reveal the spherical morphology of the $\text{SiO}_2/\text{AgNO}_3@\text{PZS}$

composite, with nanoparticles embedded on the surfaces. Examination of the cracked particle in Figure 1d reveals the presence of numerous nanoparticles filling the composite material, suggesting that these nanoparticles were uniformly dispersed throughout the entire sphere without agglomeration. The polymerization mechanism is postulated as follows. HCCP and BPS co-monomers undergo precipitation condensation reactions catalyzed by the acid-binding agent triethylamine, resulting in the formation of numerous PZS initial oligomers with varying particle sizes during the initial stages of the reaction. Owing to the low surface energy of PZS oligomers, they spontaneously adhere to the high surface energy surface of nano $\text{SiO}_2/\text{AgNO}_3$, followed by collision crosslinking between the initial coating bodies, leading to the formation of a composite material [16]. Non-polar solvents ensure the complete encapsulation of PZS oligomers around the template, thereby forming an optimal coating.

Figure 2 presents TEM images of $\text{SiO}_2/\text{Ag}@\text{PZS-C}$ after carbonization. The images reveal SiO_2/Ag nanoparticles encapsulated and confined within PZS-C carbon shells, exhibiting a carbon layer thickness ranging from 10 to 30 nm. The thinner carbon layer not only prevents direct contact between the silica active materials and the electrolyte but also reduces the migration distance of lithium ions. Additionally, the images depict the undulating and rough surface of the composite material, with a distinct porous structure internally, yet no structural collapse is observed.

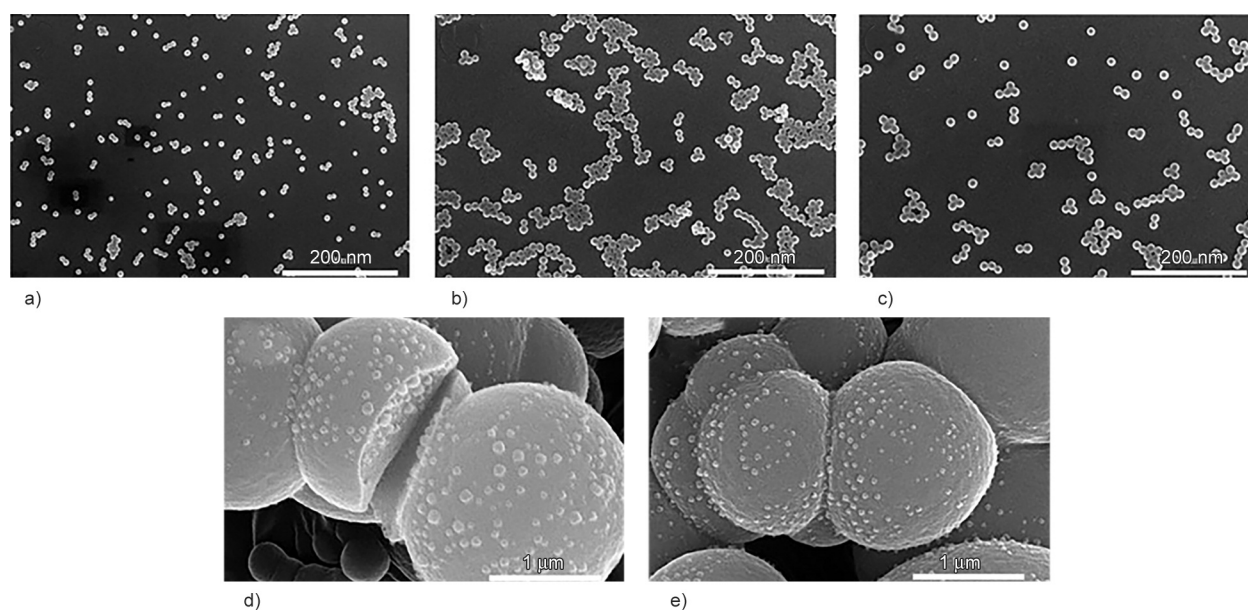


Figure 1. a)–c) SEM images of silica at increasing ammonia concentrations, d), e) SEM images of $\text{SiO}_2/\text{AgNO}_3@\text{PZS}$ composites.

High-resolution transmission electron microscopy images in **Figures 2e** reveal clear lattice fringes, with a stripe spacing of $d = 0.24$ nm measured using DigitalMicrograph software, corresponding to the (111) crystal plane of cubic silver. In **Figure 2f**, distinct lattice stripes reflected by the light and dark contrasts are observed, indicating a crystal plane spacing of $d = 0.18$ nm, corresponding to the (112) crystal plane of SiO_2 . Nevertheless, a significant portion of SiO_2 exists in an amorphous state. In contrast to the SEM images showing $\text{SiO}_2/\text{AgNO}_3$ with a nanospherical structure, the SiO_2/Ag particles observed in TEM predominantly display random morphology, possibly attributed to the decomposition of AgNO_3 during carbonization, leading to the formation of nanoAg.

Also, a gap exists between SiO_2/Ag and PZS-C, serving to alleviate the volume expansion of the negative electrode material [17, 18].

To elucidate the impact of high-temperature treatment on the material structure of $\text{SiO}_2/\text{AgNO}_3$ nanoparticles, X-ray diffraction (XRD) analysis was performed on $\text{SiO}_2/\text{AgNO}_3$ (pre-high-temperature treatment) and SiO_2/Ag (post-high-temperature treatment). As depicted in **Figure 3**, the line marked ‘unannealed SiO_2/Ag ’ is the XRD spectra of $\text{SiO}_2/\text{AgNO}_3$, the XRD spectrum of $\text{SiO}_2/\text{AgNO}_3$ exhibits a broad diffraction peak at approximately $20\text{--}30^\circ$, indicative of amorphous SiO_2 . Following high-temperature calcination, SiO_2/Ag displays a distinct characteristic peak, indicating the presence of crystalline silver.

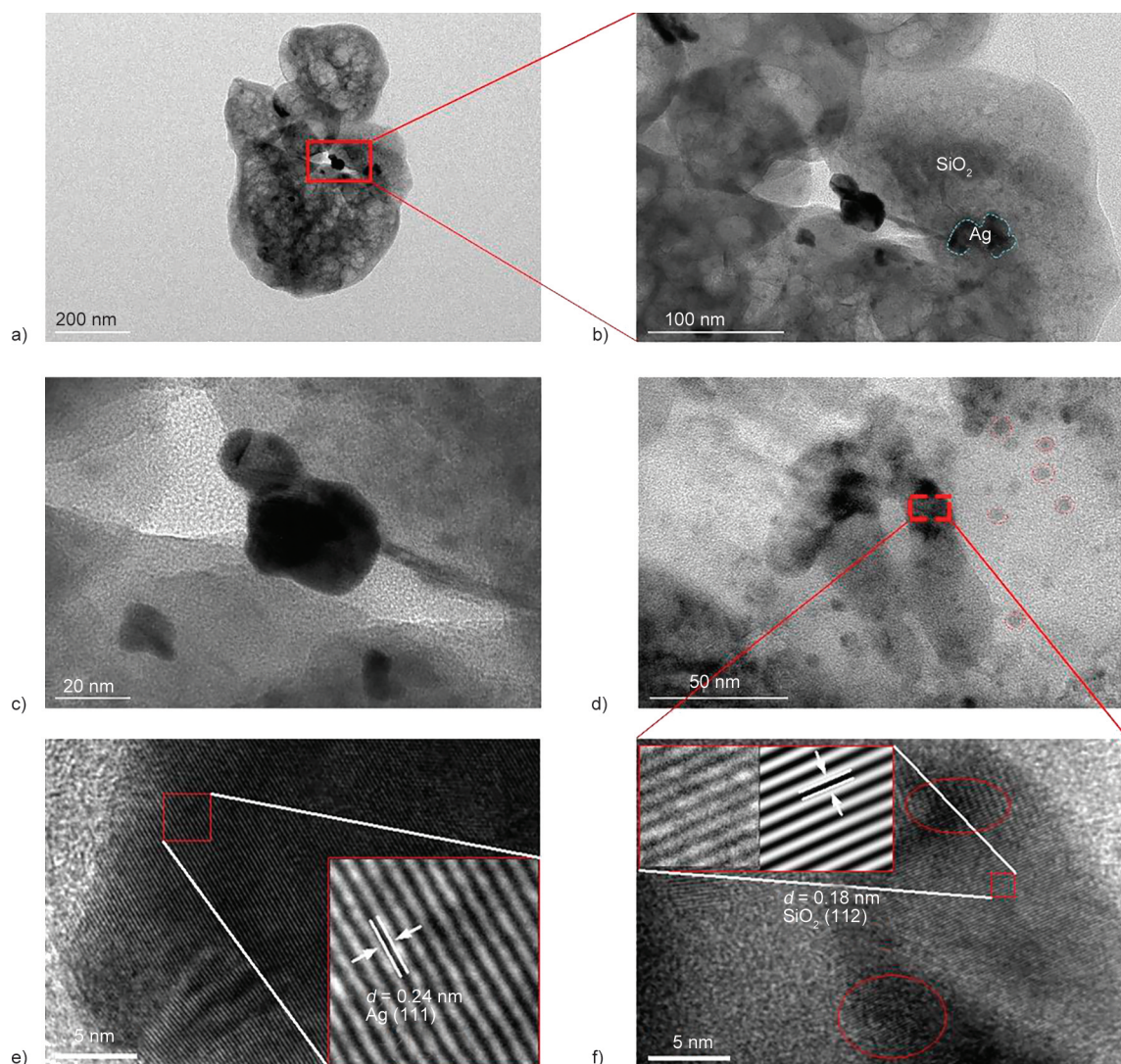


Figure 2. TEM images of $\text{SiO}_2/\text{Ag}@PZS-C$. In (f), the magnified image is embedded in the upper left corner, along with the Fourier transform analysis conducted using DigitalMicrograph. a) TEM image of sample with scale of 200 nm; b) TEM image of sample with scale of 100 nm; c) TEM image of sample with scale of 20 nm; d) TEM image of sample with scale of 50 nm; e), f) TEM images of sample with scale of 5 nm, and the magnified image is embedded in the corner, along with the Fourier transform analysis conducted using DigitalMicrograph.

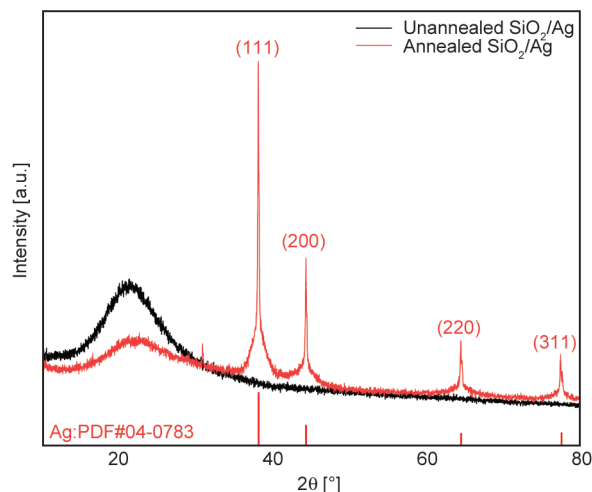


Figure 3. XRD spectra of $\text{SiO}_2/\text{AgNO}_3$ and SiO_2/Ag .

These findings indicate the successful decomposition of AgNO_3 into Ag crystals under an inert atmosphere, corroborating TEM observations.

To assess the pore structure characteristics and pore-forming mechanism of the composites, N_2 adsorption/desorption isotherm tests and thermogravimetric analysis were conducted. Figure 4 illustrates the N_2 adsorption/desorption isotherms of $\text{SiO}_2/\text{Ag}@PZS-C$, revealing mixed Type I and Type IV isotherms accompanied by H4 hysteresis loops. The specific surface area of $\text{SiO}_2/\text{Ag}@PZS-C$ was $278.08 \text{ m}^2 \cdot \text{g}^{-1}$, with an average pore size of 1.97 nm. The pore size distribution in the lower right corner indicates that the material's pore structure mainly comprises micropores less than 2 nm in diameter, with a few mesopores present. Evidently, the presence of SiO_2/Ag significantly altered the composite's pore structure, likely due to the pyrolysis of $\text{SiO}_2/\text{AgNO}_3$. The presence

of micropores in the sample substantially enhances the specific surface area and reaction sites, thereby improving its electrochemical performance [19]. Mesopores can serve as conduits for efficient ion transfer, facilitating the rapid movement of free ions and mitigating polarization induced by counter ions. Figure 4 illustrates a notable inflection point in the DTG curve around 450°C , likely attributed to the decomposition of silver nitrate on $\text{SiO}_2/\text{AgNO}_3$ nanoparticles, resulting in the formation of silver, nitrogen, and nitrogen dioxide. Moreover, the volume of SiO_2/Ag decreases after pyrolysis, creating a buffer space between SiO_2/Ag and the PZS-C coating. This leads to an increase in internal pore size, imparting a mesoporous appearance to the composite and consequently enhancing its specific surface area.

Figure 5a depicts X-ray diffraction patterns of $\text{SiO}_2@PZS-C$ and $\text{SiO}_2/\text{Ag}@PZS-C$. $\text{SiO}_2@PZS-C$ exhibited only a broad diffraction peak between 20° and 30° , resulting from the overlap of amorphous carbon and amorphous silicon dioxide. Conversely, $\text{SiO}_2/\text{Ag}@PZS-C$ exhibited prominent diffraction peaks at 38° , 44° , 64° , and 77° , corresponding to the (111), (200), (220), and (311) planes of face-centered cubic silver. The intensity of these diffraction peaks is notably high, suggesting excellent crystallinity of silver. Moreover, $\text{SiO}_2/\text{Ag}@PZS-C$ exhibited a weak characteristic peak at $2\theta = 23.7^\circ$, indicating the presence of a small amount of crystalline SiO_2 in the composite, consistent with TEM characterization.

Figure 5b presents the Raman spectra of $\text{SiO}_2@PZS-C$ and $\text{SiO}_2/\text{Ag}@PZS-C$. In the Raman spectrum of carbon materials, two obvious peaks, namely the D band and the G band, are usually observed. Due to the

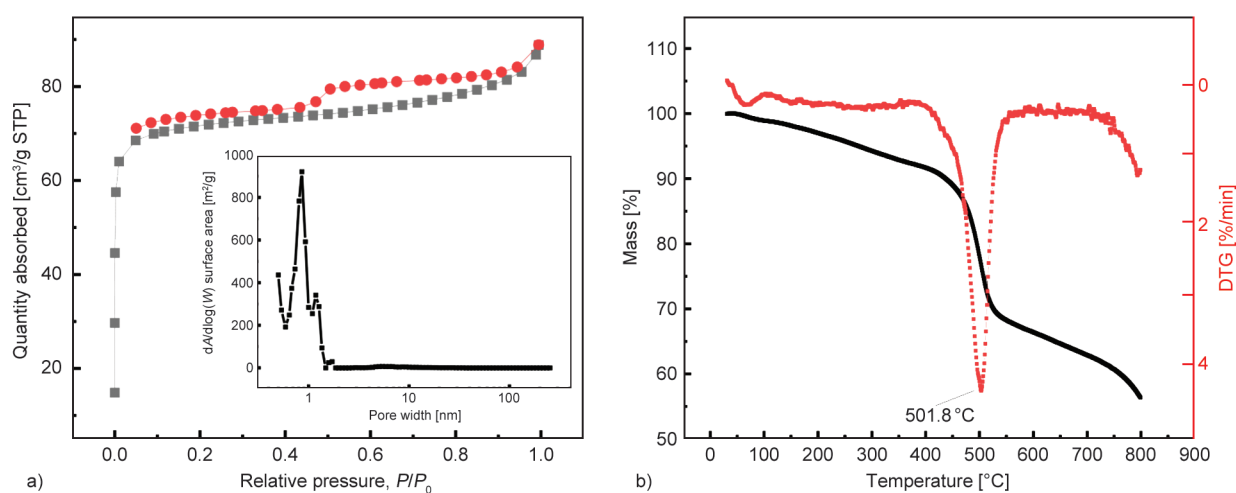


Figure 4. a) N_2 adsorption-desorption curve and pore distribution curve of $\text{SiO}_2/\text{Ag}@PZS-C$ and b) thermogravimetric (TG)/differential thermogravimetric (DTG) curve of $\text{SiO}_2/\text{Ag}@PZS-C$.

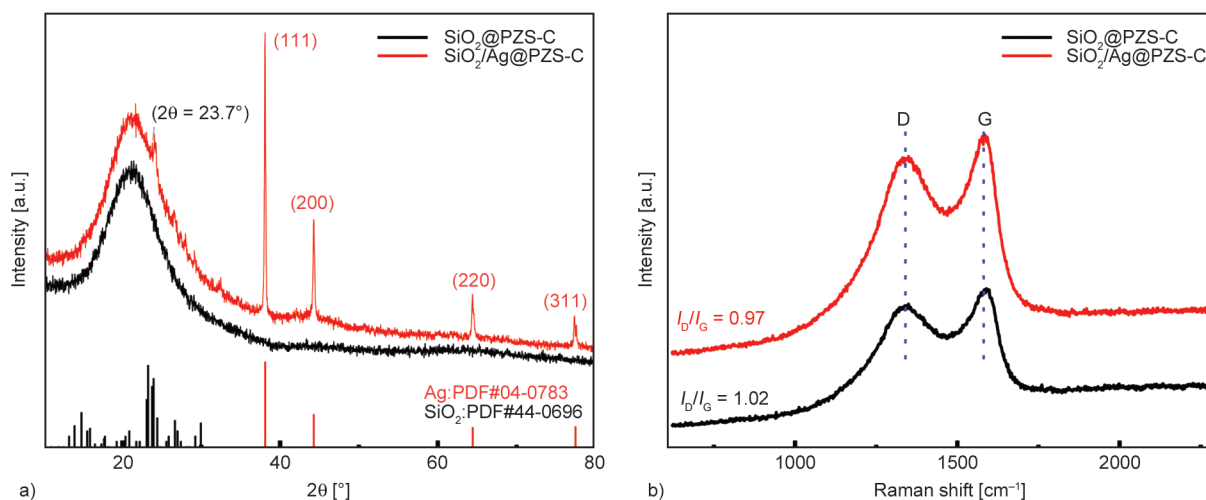


Figure 5. a) XRD patterns and b) Raman of $\text{SiO}_2\text{@PZS-C}$ and $\text{SiO}_2/\text{Ag@PZS-C}$

existence of a polyphosphazene carbon shell, Both $\text{SiO}_2\text{@PZS-C}$ and $\text{SiO}_2/\text{Ag@PZS-C}$ exhibit characteristic absorption peaks at 1327 cm^{-1} (D band) and 1575 cm^{-1} (G band), attributed to the lattice defects and graphitization of carbonized polyphosphazene carbon materials, respectively [20]. Calculations yielded an I_D/I_G value, which indicates the graphitization degree of carbon materials, of 0.97 for $\text{SiO}_2/\text{Ag@PZS-C}$. D band is related to crystal defects of carbon materials, especially edge defects and internal defects. Lattice defect regions in carbon materials, such as lamellar cavities, plate-like edges, and other amorphous microcrystal structures, can provide additional active sites for electrochemical reactions [21].

X-ray photoelectron spectroscopy (XPS) is a characterization technique used to analyze the surface chemical composition and relative abundance of materials. Figures 6 are the XPS spectra of $\text{SiO}_2/\text{Ag@PZS-C}$ and $\text{SiO}_2\text{@PZS-C}$, respectively. It is not difficult to

see that there is not much difference between the XPS spectra of the two samples, except that the spectrum of $\text{SiO}_2/\text{Ag@PZS-C}$ has an Ag 3d orbital peak more than that of $\text{SiO}_2\text{@PZS-C}$. In summary, Figure 6 displays numerous weak characteristic peaks, including Si 2p, P 2p, Si 2s, S 2p, and P 2s, ranging in binding energy from 100 to 200 eV [22]. Surface heteroatoms exhibit a closer relationship with the rate performance of electrode materials during rapid charging and discharging. The oxygen-containing functional groups can have reversible reactions with Li^+ , contributing significantly to the pseudo-capacitive energy storage of anode materials [23]. Widely used as doping elements, P and S not only increase the number of defects and active sites within the graphite carbon layer to absorb lithium ions, enhancing the conductivity and ion diffusion rate of the material but also contribute additional lithium storage capacity to the anode material through reversible pseudo-capacitance redox reactions [24, 25].

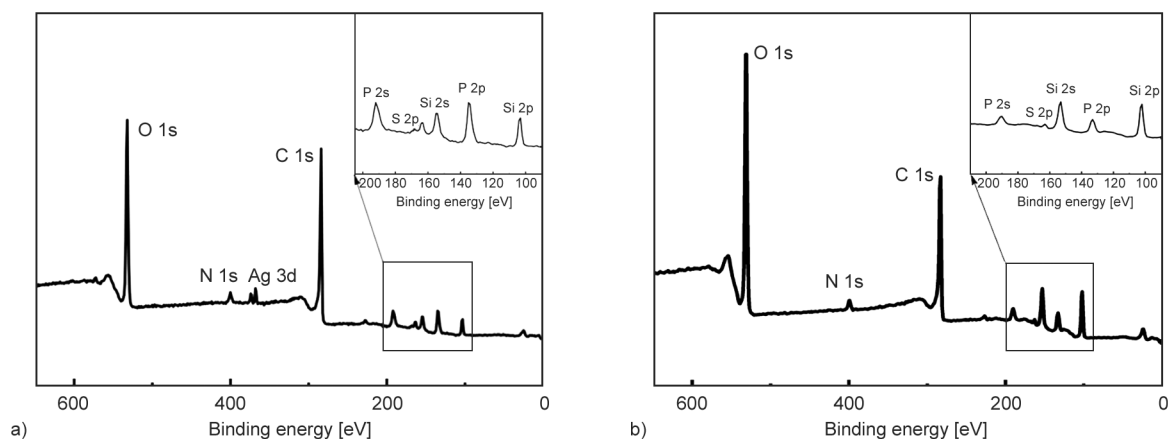


Figure 6. XPS spectra of prepared a) $\text{SiO}_2/\text{Ag@PZS-C}$ and b) $\text{SiO}_2\text{@PZS-C}$.

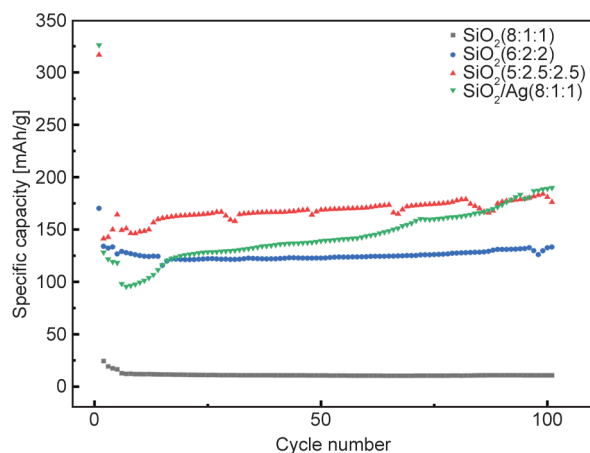


Figure 7. Lithium storage cycle performance of SiO₂ negative electrode (containing different proportions of conductive agent) and SiO₂/Ag.

3.2. Electrochemical performance characterization of SiO₂/Ag@PZS-C

Prior to electrochemical testing, the impact of conductivity on the lithium storage performance of silicon dioxide was investigated. Silica served as the active material, while acetylene black and CMC were used as the conductive agent and binder, respectively. The slurry was prepared in various ratios, namely, 8:1:1, 6:2:2, and 5:2.5:2.5, of the active material, conductive agent, and binder. The slurry was applied onto a negative electrode and subjected to constant current charge-discharge testing. [Figure 7](#) illustrates the cyclic performance of SiO₂/Ag and SiO₂. SiO₂ (8:1:1) displayed a specific capacity of merely 10 mAh·g⁻¹ without any notable electrochemical activity. With increasing conductive agent content, silica's lithium storage capacity increased from 10 mAh·g⁻¹ in SiO₂ (8:1:1) to 183 mAh·g⁻¹ in SiO₂ (5:2.5:2.5). Additionally, the cyclic capacity curve for the SiO₂ (5:2.5:2.5) negative electrode exhibited a slight upward trend. However, solely enhancing the proportion of conductive agents to boost silica's conductivity does not maximize its lithium storage capacity. Given that silver is an excellent conductive material, doping with silver has the potential to significantly enhance the electrochemical lithium storage capacity. As anticipated, doping SiO₂ with silver (SiO₂/Ag) yields a lithium storage capacity of 194 mAh·g⁻¹, twentyfold that of SiO₂ (8:1:1). This improvement is attributed to silver nanoparticles providing an efficient electronic pathway from the collector to silica's interior.

[Figures 8a](#) and [Figures 8b](#) depict the cyclic voltammetry curves of SiO₂ and SiO₂/Ag. Generally, the

two curves overlap, demonstrating comparable electrochemical behavior and thus suggesting that the inclusion of nano-Ag primarily serves as a conductive agent without directly engaging in the electrochemical reaction. Particularly, in the initial cathodic scan, a reduction peak emerged at 1.52 V for both SiO₂ and SiO₂/Ag, attributed to electrolyte decomposition. Subsequently, a huge reduction peak of SiO₂ appeared at 0.9 V and disappeared in subsequent cycles, as a large amount of SiO₂ was reduced to irreversible Li₂O and Li₄SiO₄, as well as reversible products Li₂Si₂O₅ and Si. The gradual slopes observed in the subsequent second and third cycles depict the lithium intercalation reaction involving the reversible product Li₂Si₂O₅. The reverse process of lithium removal is indicated by the oxidation peak at 1.0 V, whereby Li₂Si₂O₅ decomposes to produce Li and SiO₂. The pair of reduction and oxidation peaks at respectively 0.01 V and 0.12 V involving reaction involving the reversible products Si and Li. In [Figure 8b](#), the peak observed at 0.74 V for SiO₂/Ag is ascribed to the formation of the solid electrolyte interface (SEI) film. Notably, the intensity of the de-intercalation lithium peak in the SiO₂/Ag silicon-lithium alloy surpasses that of SiO₂, with the narrower peak indicating that silver nanoparticle doping enhances the electrochemical activity of SiO₂/Ag and facilitates the reaction.

[Figure 8c](#) illustrates the cyclic voltammetry (CV) plot of SiO₂/Ag@PZS-C. Although polyphosphazene carbon materials inherently exhibit excellent conductivity and contain abundant heteroatoms, the distinct electrochemical behavior of SiO₂ is not readily apparent due to the composite structure and the high electrochemical activity of polyphosphazene carbon. Specifically, the reduction peak at 0.1 V arises from the overlapping alloying and lithium intercalation reactions between the reduced product Si and polyphosphazene carbon. During the subsequent anodic scan, a broad oxidation peak ranging from 0.1 to 0.5 V signifies the de-lithiation of amorphous silicon-lithium alloys and the de-lithiation process of Li_xC. The broad oxidation peak at 1.1 V corresponds to the oxidation reactions of Li_xP and Li₂Si₂O₅. Due to the close proximity of the oxidation peaks, they cannot be distinctly differentiated. The CV curves of SiO₂/Ag@PZS-C after the initial cycle exhibit remarkable consistency and form closed loops. The lithium storage mechanism of SiO₂/Ag@PZS-C is described as follows:

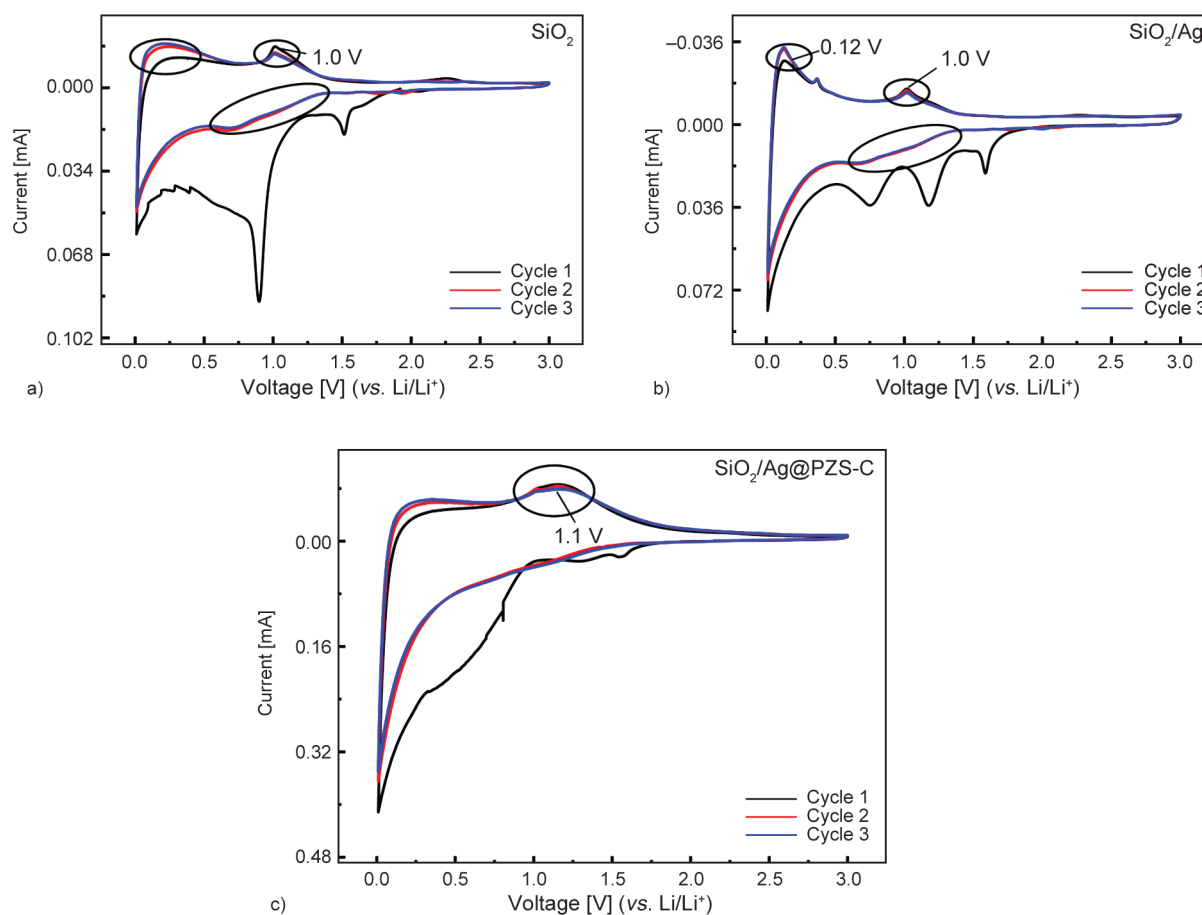


Figure 8. CV curves of a) SiO₂, b) SiO₂/Ag and c) SiO₂/Ag@PZS-C.

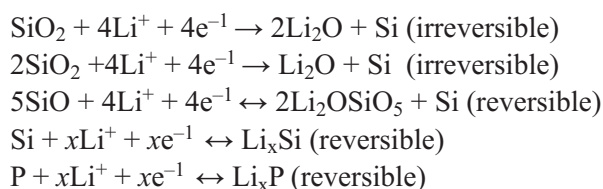


Figure 9a illustrates the cyclic test results for each sample within the voltage range of 0.01 to 3 V at a current density of 100 mA·g⁻¹. Specific cyclic performance parameters are listed in Table 1. SiO₂ material exhibited poor conductivity, resulting in a first discharge specific capacity of only 81 mA·g⁻¹ and a cyclic specific capacity of merely 10 mA·g⁻¹. However, the reversible specific capacity of SiO₂/Ag doped with silver nanoparticles increased by 18 times due to improved conductivity. SiO₂@PZS-C demonstrated good cycling stability with a capacity retention rate of up to 83.4%. This is attributed to the reduced direct contact between the SiO₂ surface and electrolyte facilitated by the outer shell PZS-C, and the enhanced conductivity of carbon materials [26]. However, the actual specific capacity of SiO₂@PZS-C remains limited, at only 338 mA·g⁻¹. Interestingly,

the specific discharge capacity of both SiO₂/Ag and SiO₂@PZS-C gradually increases with the number of cycles, possibly due to the gradual activation of the silica main body. During the insertion and removal of lithium ions, silica particles undergo rupture, enabling more fresh active substances to interact with lithium ions, consequently leading to an increase in specific capacity.

Conversely, SiO₂/Ag@PZS-C composite materials demonstrated excellent lithium storage performance, and after 100 cycles, the capacity remained at 535 mA·g⁻¹. After 400 cycles of charging and discharging, the lithium storage capacity remained at approximately 400 mA·g⁻¹, with only a 0.15% decrease in specific capacity per cycle. This excellent electrochemical performance is attributed to the dual modifications of silver nanoparticles and PZS-C coating. Silver nanoparticles provided an effective electronic channel from the current collector to the silica particles. Concurrently, PZS-C prevented direct contact between SiO₂/Ag and the electrolyte, thereby preventing the formation of unstable SEI films.

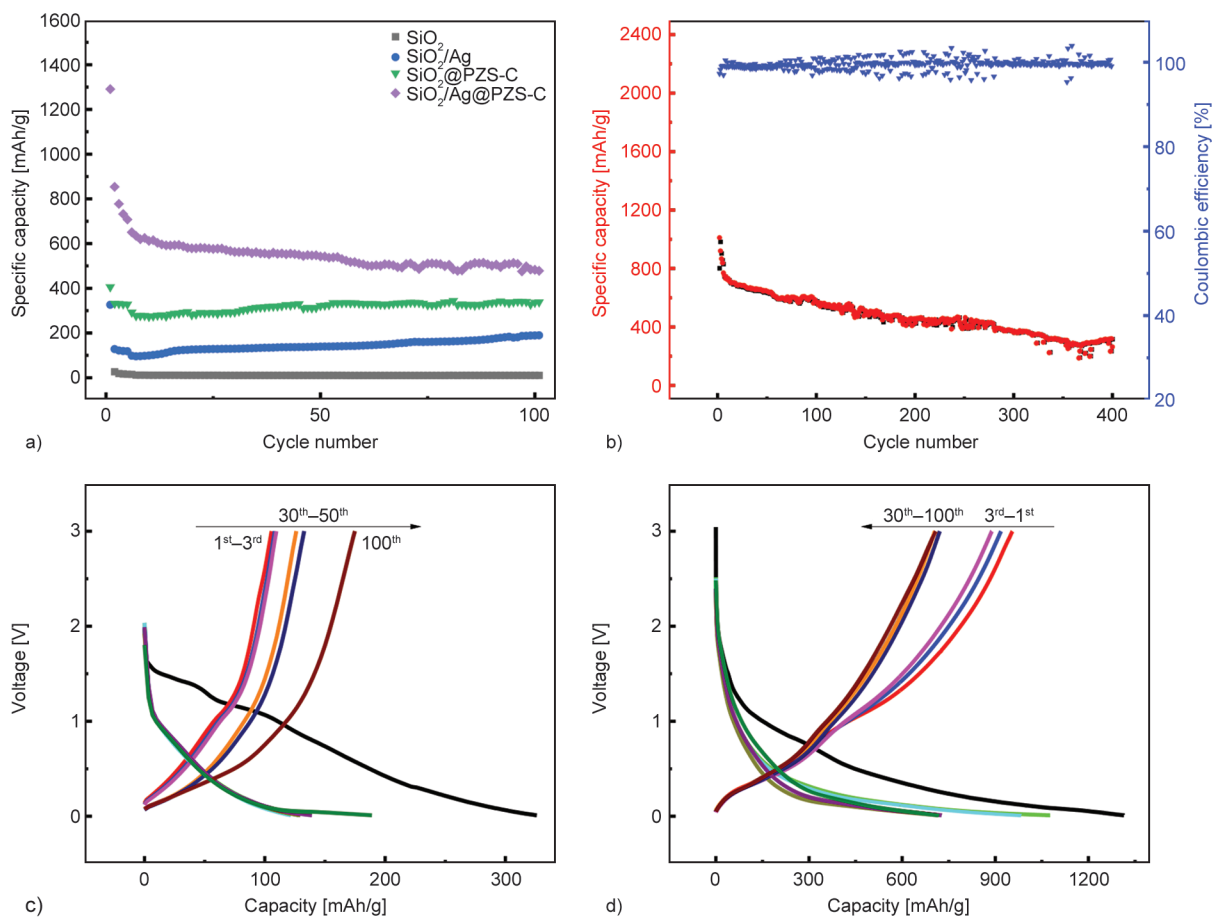


Figure 9. a) Cyclic performance of samples at 100 mA·g⁻¹ current density; b) cyclic stability performance of SiO₂/Ag@PZS-C; Galvanostatic discharge/charge profiles of c) SiO₂/Ag and d) SiO₂/Ag@PZS-C.

Table 1. Cycling performance parameters of all samples at a current density of 100 mA·g⁻¹.

Sample	Initial discharge-specific capacity [mAh·g ⁻¹]	Initial coulombic efficiency (ICE) [%]	Specific capacity after 100 cycles [mAh·g ⁻¹]
SiO ₂	81	32	10
SiO ₂ /Ag	326	32	189
SiO ₂ @PZS-C	405	77	338
SiO ₂ /Ag@PZS-C	1293	61	535

Figures 9c and Figures 9d depict the voltage-specific capacity curves of SiO₂/Ag and SiO₂/Ag@PZS-C. SiO₂/Ag exhibited its first discharge plateau near 1.5 V during the initial discharge process, attributed to electrolyte decomposition. Figure 9d reveals that, due to the presence of PZS-C, the charging platform with 0.2 V corresponding to Si had no capacity attenuation. It is worth noting that the subsequent GCD cycle shows a linear inclined discharge curve, which means that SiO₂/Ag@PZS-C had pseudo-capacitance behavior, which is expected to improve the dynamic limitation of slow solid-state diffusion of Li⁺ in active materials, thus obtaining superior performance.

Figure 10 shows the test results of the rate performance of SiO₂/Ag@PZS-C. When the current density was 1 and 2 A·g⁻¹, the lithium intercalation capacity of SiO₂/Ag@PZS-C was respectively 222 and 182 mA·g⁻¹. When the current density was reduced to 100 mA·g⁻¹ again, the specific capacity of the anode material was restored to 764 mA·g⁻¹. Upon returning the current density to 100 mA·g⁻¹, the specific capacity of the negative electrode material nearly returned to its initial level of 864 mA·g⁻¹. Furthermore, during cycling at high current density, the sample maintained a Coulombic efficiency exceeding 99.8%, indicating the excellent electrochemical stability and reversibility of SiO₂/Ag@PZS-C.

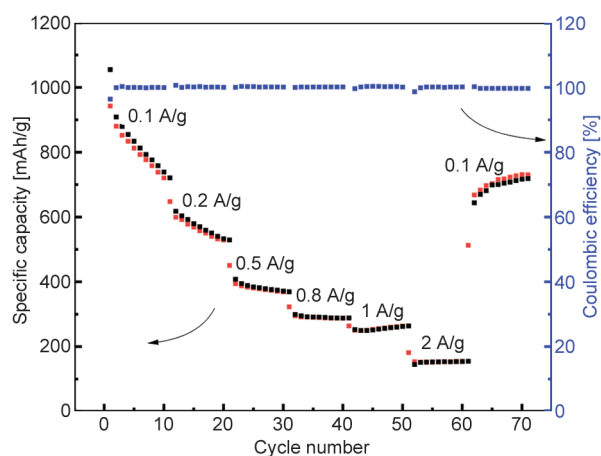


Figure 10. Rate performance of SiO₂/Ag@PZS-C.

Figure 11 displays the EIS spectra of the samples across the frequency range of 0.01~100 000 Hz. The summary of electrochemical impedance fitting results is presented in Table 2. The R_{ct} of SiO₂ was 660.7 Ω , whereas for SiO₂/Ag, SiO₂@PZS-C, and SiO₂/Ag@PZS-C, the R_{ct} values were 291.3, 175.2, and 39.7 Ω , respectively. This demonstrates that the doping of silver nanoparticles and the coating with PZS-C significantly decreased the transfer resistance of lithium ions at the electrode material interface. The high conductivity of silver nanoparticles and polyphosphazene carbon shell is characterized by fast electron and ion transport kinetics, which improves the charging and discharging efficiency, cycle life and capacity retention rate of the battery [27, 28]. Compared with other precious metals such as platinum and gold, silver is a widely existing and recyclable metal, and it is more economical to use silver nanoparticles as electrode modification materials. As a new method to modify electrode materials, the successful application of polyphosphazene carbonized

Table 2. EIS results of all samples.

Sample	R_s [Ω]	R_{SEI} [Ω]	R_{ct} [Ω]
SiO ₂	7.9	257.5	660.7
SiO ₂ /Ag	7.3	10.8	291.3
SiO ₂ @PZS-C	7.1	6.3	175.2
SiO ₂ /Ag@PZS-C	6.8	3.6	39.7

shell provides a new way to develop high-performance batteries [29]. Using silver nanoparticles and polyphosphazene carbon as electrode modification materials is helpful in promoting the environmental protection and sustainable development of battery technology.

To delve deeper into the characteristics of SiO₂/Ag@PZS-C, the Li⁺ storage mechanism of negative electrode materials was elucidated via CV scanning, thereby discerning the ratio of diffusion behavior to pseudocapacitance contribution to the overall capacity during lithium storage. Figure 12a shows the CV curves of composite materials at different scanning speeds [23, 30]. Notably, SiO₂/Ag@PZS-C gave an oxidation peak b value of 0.71 at 1 V (Figure 12b). This suggests that the capacity of SiO₂/Ag@PZS-C during lithium storage is attributed to pseudocapacitive behavior [31].

Using the CV curve obtained at a scanning rate of 1 mV·s⁻¹ as an example in Figure 12c, the red area signifies the capacitive effect, while the blank area corresponds to diffusion-controlled capacity. The capacitance curve displays prominent pseudo-capacitance peaks, which account for 34% of the total area. As illustrated in Figure 12d, despite the energy storage mechanism being primarily dictated by battery lithium storage, the contribution of capacitance

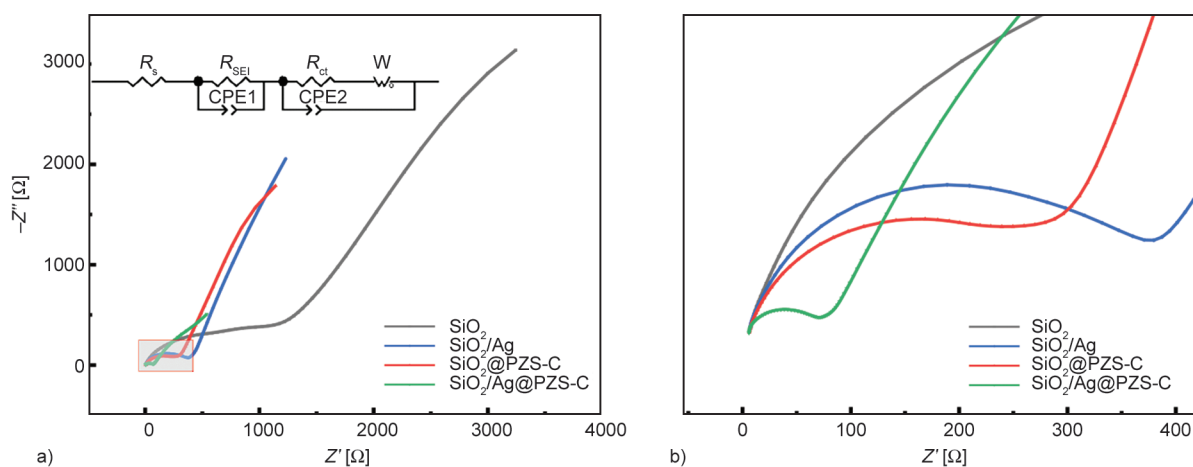


Figure 11. a) EIS spectrum of samples; b) zoomed-in view at the high-frequency region.

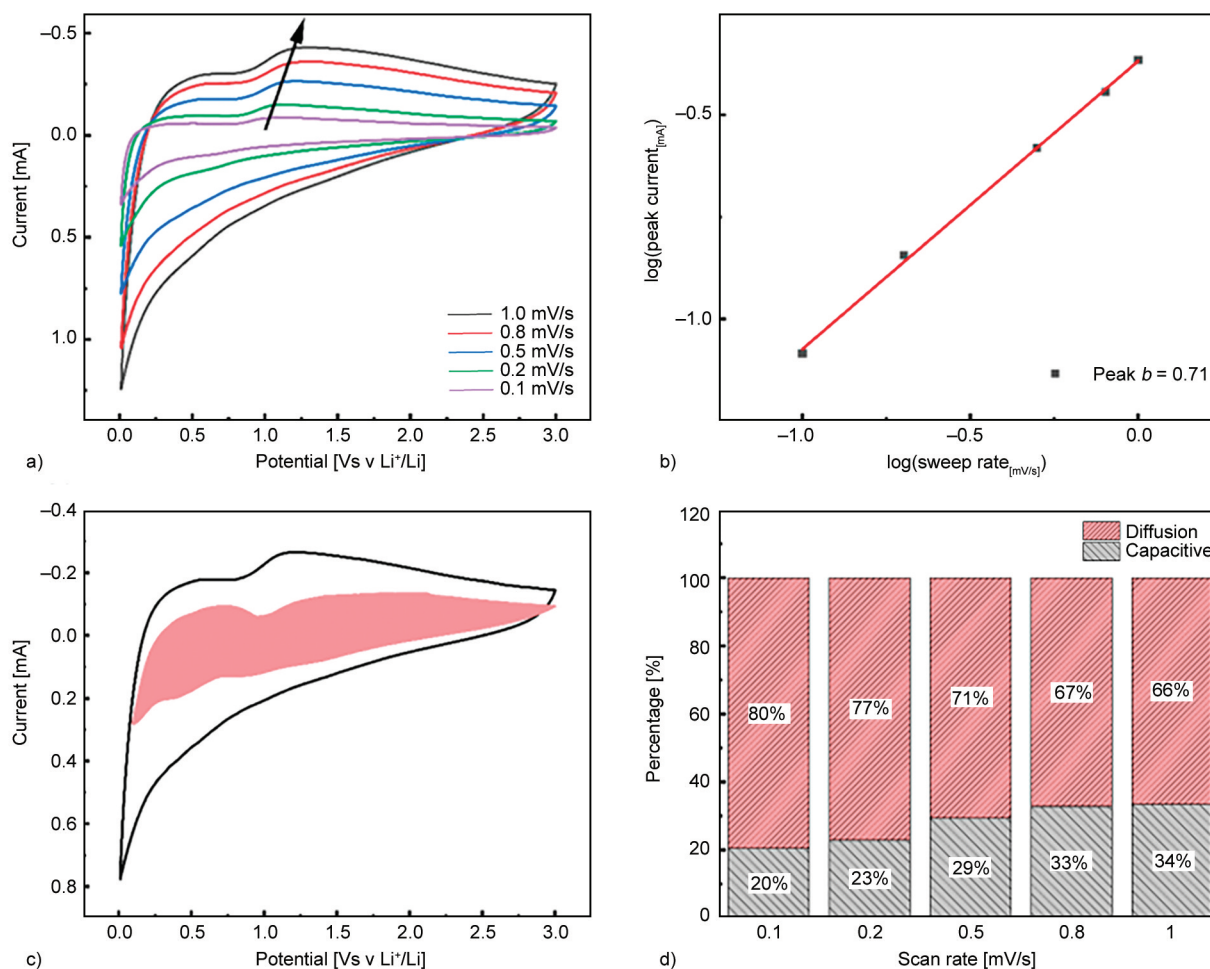


Figure 12. Electrochemical properties of the $\text{SiO}_2/\text{Ag@PZS-C}$ electrode: a) CV curves at various scan rates; b) correlations between peak current and sweep rate during charging/discharging; c) CV response at a scan rate of 1 $\text{mV}\cdot\text{s}^{-1}$ (capacitive contribution is marked by red region); d) percentages of capacitive contribution at different scan rates.

progressively rises with the scanning rate. The abundance of hetero element groups, crystallographic defects, and dangling bonds on the surface of polyphosphazene carbon can engage in capacitive electrochemical behavior with lithium ions, thus steering the battery performance towards pseudo-capacitive lithium storage.

The complexity of pseudocapacitive materials' electrochemical interfaces necessitates the consideration of various physical and chemical processes, such as ion diffusion, double-layer formation, charge transfer, and intercalation reactions, rendering their modeling a significant challenge. It is necessary to understand the electrochemical behavior controlled by electrode potential, scanning rate, and ion diffusion by solving electronic dynamics equations such as the Butler-Volmer equation and Poisson-Nernst-Planck equation based on simulated real devices. Given that this topic exceeds the scope of the current article, further discussion will not be provided.

Table 3 provides a summary of the electrochemical performance from other high-performance data in the literature for comparative analysis. The synthesized $\text{SiO}_2/\text{Ag@PZS-C}$ demonstrated an extraordinary initial capacity of $1293 \text{ mAh}\cdot\text{g}^{-1}$ and maintained a capacity of $535 \text{ mAh}\cdot\text{g}^{-1}$ after 100 cycles, indicating superior lithium storage performance in comparison to previous literature reports.

4. Conclusions

In this study, silver nanoparticles and carbon coating were proposed for the dual modification of nano- SiO_2 , leading to the successful fabrication of $\text{SiO}_2/\text{Ag@PZS-C}$ composite materials.

Electrochemical tests reveal the exceptional lithium storage performance of $\text{SiO}_2/\text{Ag@PZS-C}$ composite materials. At a current density of $0.1 \text{ A}\cdot\text{g}^{-1}$, the initial discharge-specific capacity was $2293 \text{ mAh}\cdot\text{g}^{-1}$, and after 400 cycles, the lithium storage capacity still remained at approximately $400 \text{ mAh}\cdot\text{g}^{-1}$.

Table 3. Summary of electrochemical performances of Si-based anodes reported in comparison with this work.

Materials	Initial specific capacity (Current density)	Initial coulombic efficiency	Reversible specific capacity (Cycles)	References
3D-SiO ₂ @C	~1250 mAh·g ⁻¹ (500 mAh·g ⁻¹)	~50%	687.7 mAh·g ⁻¹ (1000)	[32]
PDA-PEI@PVP-SiO ₂ @Si	719 mAh·g ⁻¹ (100 mAh·g ⁻¹)	47.94%	539 mAh·g ⁻¹ (100)	[33]
SiO ₂ -SiO ₂ @C	1566.6 mAh·g ⁻¹ (200 mAh·g ⁻¹)	75.73%	1061 mAh·g ⁻¹ (100)	[34]
SiO ₂ nanotubes	625.5 mAh·g ⁻¹ (40 mAh·g ⁻¹)	49.7%	232.5 mAh·g ⁻¹ (100)	[35]
SiO ₂ /C composite fibers	740.3 mAh·g ⁻¹ (50 mAh·g ⁻¹)	68%	465 mAh·g ⁻¹ (50)	[36]
SiO ₂ /TiO ₂ @C nanosheets	1016 mAh·g ⁻¹ (100 mAh·g ⁻¹)	66%	998 (100)	[37]
Nanofibrous SiO ₂ /C composite	1582 mAh·g ⁻¹ (100 mAh·g ⁻¹)	45.9%	400.4 (100)	[13]
SiO ₂ /Ag@PZS-C	1293 mAh·g ⁻¹ (100 mAh·g ⁻¹)	61%	535 (100)	This work

Electrochemical impedance spectroscopy (EIS) results indicate a decrease in the R_{ct} of the negative electrode from 660.7 Ω for SiO₂ to 3.6 Ω for SiO₂/Ag@PZS-C.

The excellent electrochemical properties of SiO₂/Ag@PZS-C composites are attributed to the synergistic effect of nano-silver and polyphosphazene carbon. Polyphosphazene porous carbon shell has a high level of multi-element doping, including nitrogen, oxygen, phosphorus and sulfur, which provide a considerable number of active sites. Also, the internal porous structure of polyphosphazene provided expansion space, which played a role in buffering the volume change of SiO₂ and improving the structural stability. Silver nanoparticles greatly improve the conductivity of the material and reduce the charge transfer resistance, which plays a great role in the charge-discharge efficiency, cycle life and capacity retention of the battery.

Acknowledgements

We are thankful for the Project Supported by Zhejiang Provincial Natural Science Foundation of China (LY21C160007) and National Natural Science Foundation of China (21504079) for the support to this research.

References

- [1] Wang H., Yang X., Wu Q., Zhang Q., Chen H., Jing H., Wang J., Mi S-B., Rogach A. L., Niu C.: Encapsulating silica/antimony into porous electrospun carbon nanofibers with robust structure stability for high-efficiency lithium storage. *ACS Nano*, **12**, 3406–3416 (2018).
<https://doi.org/10.1021/acsnano.7b09092>

- [2] Li W., Wang F., Ma M., Zhou J., Liu Y., Chen Y.: Preparation of SiO₂ nanowire arrays as anode material with enhanced lithium storage performance. *RSC Advances*, **8**, 33652–33658 (2018).
<https://doi.org/10.1039/C8RA06381H>
- [3] Zhou J., Xu R., Yin C., Li Z., Wu W., Wu M.: *In situ* growth of polyphosphazene nanoparticles on graphene sheets as a highly stable nanocomposite for metal-free lithium anodes. *RSC Advances*, **6**, 62005–62010 (2016).
<https://doi.org/10.1039/C6RA11597G>
- [4] Ali Z., Basharat M., Wu Z.: A review on the morphologically controlled synthesis of polyphosphazenes for electrochemical applications. *ChemElectroChem*, **8**, 759–782 (2021).
<https://doi.org/10.1002/celec.202001352>
- [5] Romanyuk A., Wang R., Marin A., Janus B. M., Felner E. I., Xia D., Goez-Gazi Y., Alfson K. J., Yunus A. S., Toth E. A., Ofek G., Carrion R., Prausnitz M. R., Fuerst T. R., Andrianov A. K.: Skin vaccination with ebola virus glycoprotein using a polyphosphazene-based microneedle patch protects mice against lethal challenge. *Journal of Functional Biomaterials*, **14**, 16–30 (2023).
<https://doi.org/10.3390/jfb14010016>
- [6] Rhili K., Chergui S., ElDouhaibi A. S., Mazzah A., Sijaj M.: One-pot synthesis of cyclomatrix-type polyphosphazene microspheres and their high thermal stability. *ACS Omega*, **8**, 9137–9144 (2023).
<https://doi.org/10.1021/acsomega.2c06394>
- [7] Lee S. B., Song S-C., Jin J-I., Sohn Y. S.: Structural and thermosensitive properties of cyclotriphosphazenes with poly(ethylene glycol) and amino acid esters as side groups. *Macromolecules*, **34**, 7565–7569 (2001).
<https://doi.org/10.1021/ma010648b>
- [8] Mujumdar A. N., Young S. G., Merker R. L., Magill J. H.: A study of solution polymerization of polyphosphazenes. *Macromolecules*, **23**, 14–21 (1990).
<https://doi.org/10.1021/ma00203a004>

- [9] Liu W., Zhang S., Dar S. U., Zhao Y., Akram R., Zhang X., Jin S., Wu Z., Wu D.: Polyphosphazene-derived heteroatoms-doped carbon materials for supercapacitor electrodes. *Carbon*, **129**, 420–427 (2018).
<https://doi.org/10.1016/j.carbon.2017.12.016>
- [10] Huang S., Yang D., Zhang W., Qiu X., Li Q., Li C.: Dual-templated synthesis of mesoporous lignin-derived honeycomb-like porous carbon/SiO₂ composites for high-performance Li-ion battery. *Microporous and Mesoporous Materials*, **317**, 111004 (2021).
<https://doi.org/10.1016/j.micromeso.2021.111004>
- [11] Tang C., Liu Y., Xu C., Zhu J., Wei X., Zhou L., He L., Yang W., Mai L.: Ultrafine nickel-nanoparticle-enabled SiO₂ hierarchical hollow spheres for high-performance lithium storage. *Advanced Functional Materials*, **28**, 1704561 (2018).
<https://doi.org/10.1002/adfm.201704561>
- [12] Yoo S., Lee J-I., Ko S., Park S.: Highly dispersive and electrically conductive silver-coated Si anodes synthesized via a simple chemical reduction process. *Nano Energy*, **2**, 1271–1278 (2013).
<https://doi.org/10.1016/j.nanoen.2013.06.006>
- [13] Jia D., Wang K., Huang J.: Filter paper derived nanofibrous silica-carbon composite as anodic material with enhanced lithium storage performance. *Chemical Engineering Journal*, **317**, 673–686 (2017).
<https://doi.org/10.1016/j.cej.2017.02.109>
- [14] Li S., Huang J.: A nanofibrous silver-nanoparticle/titania/carbon composite as an anode material for lithium ion batteries. *Journal of Materials Chemistry A*, **3**, 4354–4360 (2015).
<https://doi.org/10.1039/C4TA06562J>
- [15] Pidaparthy S., Luo M., Rodrigues M-T. F., Zuo J-M., Abraham D. P.: Physicochemical heterogeneity in silicon anodes from cycled lithium-ion cells. *ACS Applied Materials and Interfaces*, **14**, 38660–38668 (2022).
<https://doi.org/10.1021/acsami.2c06991>
- [16] Qiu S., Xing W., Feng X., Yu B., Mu X., Yuen R. K. K., Hu Y.: Self-standing cuprous oxide nanoparticles on silica@polyphosphazene nanospheres: 3D nanostructure for enhancing the flame retardancy and toxic effluents elimination of epoxy resins *via* synergistic catalytic effect. *Chemical Engineering Journal*, **309**, 802–814 (2017).
<https://doi.org/10.1016/j.cej.2016.10.100>
- [17] Hong D. G., Jeong D., Koong C. Y., Han Y-E., Lee H., Lee J-C.: Ion-conducting cross-linked polyphosphazene binders for high-performance silicon anodes in lithium-ion batteries. *ACS Applied Polymer Materials*, **5**, 2617–2627 (2023).
<https://doi.org/10.1021/acsapm.2c02204>
- [18] Huang J., Li Z., Liu F., Wei W., Xu X., Liu Z.: Preparation of micron-sized silicon monoxide (SiO_x)@carbon nanotube (CNT)/polymethyl methacrylate (PMMA) composite capsules as Li-ion battery anodes via a novel pickering emulsion template method. *Powder Technology*, **430**, 118911 (2023).
<https://doi.org/10.1016/j.powtec.2023.118911>
- [19] Xing B., Zeng H., Huang G., Jia J., Yuan R., Zhang C., Sun Q., Cao Y., Chen Z., Liu B.: Magnesium citrate induced growth of noodle-like porous graphitic carbons from coal tar pitch for high-performance lithium-ion batteries. *Electrochimica Acta*, **376**, 138043 (2021).
<https://doi.org/10.1016/j.electacta.2021.138043>
- [20] Zhang P., Fan J., Wang Y., Dang Y., Heumann S., Ding Y.: Insights into the role of defects on the raman spectroscopy of carbon nanotube and biomass-derived carbon. *Carbon*, **222**, 118998 (2024).
<https://doi.org/10.1016/j.carbon.2024.118998>
- [21] Zhou Z., Chen F., Wu L., Kuang T., Liu X., Yang J., Fan P., Fei Z., Zhao Z., Zhong M.: Heteroatoms-doped 3D carbon nanosphere cages embedded with MoS₂ for lithium-ion battery. *Electrochimica Acta*, **332**, 135490 (2020).
<https://doi.org/10.1016/j.electacta.2019.135490>
- [22] Kalidas N., Shen X., Yuan M., Zhao X., Lehto V-P.: Controlled surface oxidation of mesoporous silicon microparticles to achieve a stable Si/SiO_x anode for lithium-ion batteries. *Microporous and Mesoporous Materials*, **344**, 112243 (2022).
<https://doi.org/10.1016/j.micromeso.2022.112243>
- [23] Niu J., Shao R., Liu M., Liang J., Zhang Z., Dou M., Huang Y., Wang F.: Porous carbon electrodes with battery-capacitive storage features for high performance Li-ion capacitors. *Energy Storage Materials*, **12**, 145–152 (2018).
<https://doi.org/10.1016/j.ensm.2017.12.012>
- [24] Kiciński W., Szala M., Bystrzejewski M.: Sulfur-doped porous carbons: Synthesis and applications. *Carbon*, **68**, 1–32 (2014).
<https://doi.org/10.1016/j.carbon.2013.11.004>
- [25] Jiang Y., Han R., Dong J., Yu R., Tan S., Xiong F., Wei Q., Wang J., Cui L., Tian H., Yang Y., An Q.: Uncovering the origin of surface-redox pseudocapacitance of molybdenum phosphides enables high-performance flexible sodium-ion capacitors. *Chemical Engineering Journal*, **475**, 145962 (2023).
<https://doi.org/10.1016/j.cej.2023.145962>
- [26] Petrény R., Bezerédi Á., Mészáros L.: Electrically conductive polymer composites: Today's most versatile materials? *Express Polymer Letters*, **18**, 673–674 (2024).
<https://doi.org/10.3144/expresspolymlett.2024.49>

- [27] Ye J., Gao X., Wang Z., An J., Wang Y., Liu Q., Kong Z., Qi J., Wang Z., Li W., Song J., Xia G.: Difunctional ag nanoparticles with high lithiophilic and conductive decorate on core-shell SiO₂ nanospheres for dendrite-free lithium metal anodes. *Journal of Colloid and Interface Science*, **659**, 21–30 (2024).
<https://doi.org/10.1016/j.jcis.2023.12.131>
- [28] Pang B., Yang T., Wu Z., Li Z., Jin Z., Zhang W., Xia Y., Huang H., He X., Gan Y., Xia X., Zhang J.: Li_{5.5}PS_{4.5}Cl_{1.5}-based all-solid-state battery with a silver nanoparticle-modified graphite anode for improved resistance to overcharging and increased energy density. *ACS Applied Materials and Interfaces*, **16**, 20510–20519 (2024).
<https://doi.org/10.1021/acsami.4c01172>
- [29] Zhao Z., Xu Z., Chen J., Zhong M., Wang J., Chew J. W.: A review on functional applications of polyphosphazenes as multipurpose material for lithium-ion batteries. *Journal of Energy Storage*, **85**, 111049 (2024).
<https://doi.org/10.1016/j.est.2024.111049>
- [30] Li H., Lang J., Lei S., Chen J., Wang K., Liu L., Zhang T., Liu W., Yan X.: A high-performance sodium-ion hybrid capacitor constructed by metal-organic framework-derived anode and cathode materials. *Advanced Functional Materials*, **28**, 1800757 (2018).
<https://doi.org/10.1002/adfm.201800757>
- [31] Wang L., Liu F., Pal A., Ning Y., Wang Z., Zhao B., Bradley R., Wu W.: Ultra-small Fe₃O₄ nanoparticles encapsulated in hollow porous carbon nanocapsules for high performance supercapacitors. *Carbon*, **179**, 327–336 (2021).
<https://doi.org/10.1016/j.carbon.2021.04.024>
- [32] Duan X., Yu J., Liu Y., Lan Y., Zhou J., Lu B., Zan L., Fan Z., Zhang L.: A highly conductive and robust micrometre-sized SiO anode enabled by an *in situ* grown CNT network with a safe petroleum ether carbon source. *Physical Chemistry Chemical Physics*, **26**, 12628–12637 (2024).
<https://doi.org/10.1039/D4CP00116H>
- [33] Martino A., Jeon J., Park H-H., Lee H., Lee C-S.: Bubble wrap-like carbon-coated rattle-type silica@silicon nanoparticles as hybrid anode materials for lithium-ion batteries via surface-protected etching. *Batteries*, **10**, 53 (2024).
<https://doi.org/10.3390/batteries10020053>
- [34] Hu X., Xu P., Liao M., Lu X., Shen G., Zhong C., Zhang M., Huang Q., Su Z.: Amorphous SiO₂ nanoparticles encapsulating a SiO anode with strong structure for high-rate lithium-ion batteries. *ACS Applied Energy Materials*, **7**, 774–784 (2024).
<https://doi.org/10.1021/acsaeam.3c02879>
- [35] Tang J., Dai X., Wu F., Mai Y., Wang X., Jin H., Gu Y., Xie Y.: A simple and efficient one-pot synthesis of SiO₂ nanotubes with stable structure and controlled aspect ratios for anode materials of lithium-ion batteries. *Ionics*, **26**, 639–648 (2020).
<https://doi.org/10.1007/s11581-019-03246-4>
- [36] Ren Y., Yang B., Wei H., Ding J.: Electrospun SiO₂/C composite fibers as durable anode materials for lithium ion batteries. *Solid State Ionics*, **292**, 27–31 (2016).
<https://doi.org/10.1016/j.ssi.2016.05.002>
- [37] Zhang L., Gu X., Yan C., Zhang S., Li L., Jin Y., Zhao S., Wang H., Zhao X.: Titanosilicate derived SiO₂/TiO₂@C nanosheets with highly distributed TiO₂ nanoparticles in SiO₂ matrix as robust lithium ion battery anode. *ACS Applied Materials and Interfaces*, **10**, 44463–44471 (2018).
<https://doi.org/10.1021/acsami.8b16238>